# Recommender system for ablation lines to treat complex atrial tachycardia

Muhamed Vila [a,1], Massimo W. Rivolta [a,1,*], Cristian A. Barrios Espinosa [b], Laura A. Unger [b], Armin Luik [c], Axel Loewe [b], Roberto Sassi [a]

[a] *Università degli Studi di Milano, Via Celoria 18, Milan, 20133, Italy*
[b] *Institute of Biomedical Engineering, Karlsruhe Institute of Technology (KIT), Kaiserstr. 12, Karlsruhe, 76131, Germany*
[c] *Medizinische Klinik IV, Städtisches Klinikum Karlsruhe, Moltkestraße 90, Karlsruhe, 76133, Germany*

## ARTICLE INFO

## ABSTRACT

*Background and Objective:* Planning the optimal ablation strategy for the treatment of complex atrial tachycardia (CAT) is a time consuming task and is error-prone. Recently, directed network mapping, a technology based on graph theory, proved to efficiently identify CAT based solely on data of clinical interventions. Briefly, a directed network was used to model the atrial electrical propagation and reentrant activities were identified by looking for closed-loop paths in the network. In this study, we propose a recommender system, built as an optimization problem, able to suggest the optimal ablation strategy for the treatment of CAT.

*Methods:* The optimization problem modeled the optimal ablation strategy as that one interrupting all reentrant mechanisms while minimizing the ablated atrial surface. The problem was designed on top of directed network mapping. Considering the exponential complexity of finding the optimal solution of the problem, we introduced a heuristic algorithm with polynomial complexity. The proposed algorithm was applied to the data of i) 6 simulated scenarios including both left and right atrial flutter; and ii) 10 subjects that underwent a clinical routine.

*Results:* The recommender system suggested the optimal strategy in 4 out of 6 simulated scenarios. On clinical data, the recommended ablation lines were found satisfactory on 67% of the cases according to the clinician's opinion, while they were correctly located in 89%. The algorithm made use of only data collected during mapping and was able to process them nearly real-time.

*Conclusions:* The first recommender system for the identification of the optimal ablation lines for CAT, based solely on the data collected during the intervention, is presented. The study may open up interesting scenarios for the application of graph theory for the treatment of CAT.

© 2023 Published by Elsevier B.V.

## 1. Introduction

Patients suffering from complex atrial tachycardia (CAT) generally respond poorly to antiarrhythmic drugs, and catheter ablation is today recognized as the treatment of choice [1]. A typical ablation therapy starts with electro-anatomical mapping of the atrial surface affected by the CAT in the electrophysiology (EP) laboratory. The mapping may reveal the electrical activity, focal or reentrant or both, sustaining the CAT and it is instrumental for the optimal planning of the therapy. The planning is currently supported by different means of visualization of several tissue properties, typically color-coded and shown on the geometrical model of the atrium/atria reconstructed during mapping. The most used ones are activation, low voltage and phase maps, where activation times of the electrical activity, amplitude of the bipolar electrogram, and instantaneous phase are quantified. However, the noise intrinsically present in endocavitary recordings can heavily corrupt the maps and thus may hamper the planning of the ablation [2,3].

Very recently, a novel approach has been proposed to characterize the electrical propagation on the atrial tissue while also considering the geometrical aspects of the atrium/atria. The approach makes use of graph theory to create a directed graph/network model [4,5] and was called directed graph/network mapping. The

* Corresponding author.
*E-mail address:* massimo.rivolta@unimi.it (M.W. Rivolta).
[1] MV and MWR contributed to the work equally and should be regarded as co-first authors.

main advantage of modeling the electrical activity using a directed network is the fact that a plethora of efficient algorithms already exist to "query" and analyze the model in the field of graph theory. For example, one may be interested in identifying focal or reentrant activities sustaining the CAT. These activities are identified in the network as those nodes having their indegree equal to 0 or by detecting close-loop paths, *i.e.*, cycles.

The potential of this technology has recently been demonstrated for the identification of driving mechanisms of CAT [6]. Van Niewenhuyse et al. evaluated the diagnostic accuracy of the directed graph mapping with respect to the one performed by experts based on a state-of-the-art technology, *i.e.*, high density activation mapping. They found that network mapping could outperform the latter for specific types of CAT (*e.g.*, localized reentry), whereas for macroreentries, the directed network performed similar to experts. The feasibility of this technology in identifying CAT was recently confirmed using a similar methodology by our team as well [5].

So far, however, no one has investigated on the potential of directed network mapping in supporting the planning of the ablation treatment for CAT. Specifically, here we define "support" as suggesting a set of possible ablation lines suitable to terminate reentrant activities, recommended automatically by a computer program. To the best of our knowledge, only very few studies [7,8] investigated the use of graph theory for the characterization of the atrial tissue. However, they were focused on atrial fibrillation (AF), a different atrial arrhythmia, and did not consider automatic ablation planning. Personalized ablation therapies were instead investigated in other studies using machine learning [9,10], high-definition computerized simulations [11–13], or by a combined approach between simulations and graph theory [14].

In this study, we propose the first method to recommend an ablation strategy in the form of optimal ablation lines for the treatment of reentrant CAT using directed network mapping. The algorithm has been tested on computerized electro-anatomical simulations of left and right atria under different tachycardia patterns. Then, data from EP studies collected during catheter ablations were employed to evaluate the performance of the proposed algorithm.

## 2. Methods

### 2.1. Directed network mapping

In our recent works [5,15], we proposed to model the electrical propagation on the atrial tissue using a directed network $G_{prop} = (V_{prop}, E_{prop})$. The network was composed of nodes $V_{prop}$ and edges $E_{prop}$, where nodes refer to specific locations across the entire atrial surface and edges represent the presence of electrical propagation from one node towards another one.

The network was built using the electrical potentials and geometrical atrial model acquired during the sequential mapping performed during an EP study. In particular, the unipolar potentials were stored into the matrix $\tilde{\Phi}_{e,n}$ where $e$ refers to an electrode of the available catheters and $n$ to the time index. The position of the electrodes at each time index was also available and stored into the vector $\tilde{\mathbf{p}}_{e,n} = [x_n, y_n, z_n]$ where $x_n$, $y_n$ and $z_n$ are the 3-dimensional coordinates. The geometrical model was provided by the mapping system as a triangular mesh.

The first step was to create the nodes of the network $G_{prop}$. This operation was done by selecting $M$ nodes in the mesh approximately equally spaced. The position of each node was stored into the vector $\mathbf{p}_i = [x, y, z]$ containing the $x$, $y$ and $z$ coordinates for the $i$th node. After the selection, the Delaunay triangulation technique was applied to define the set of neighbors for each node $i$, hereafter mathematically defined as $\mathcal{B}_i$. All nodes connected to the node $i$ through a triangle were considered as neighbors.

**Table 1**
List of simulated AFL mechanisms. CW=clockwise, CCW=counterclockwise.

| No. | Atrium | Mechanism | Position | Direction |
|---|---|---|---|---|
| 1 | Right | Macroreentry | Tricuspid valve | CCW |
| 2 | Right | Macroreentry | Tricuspid valve | CW |
| 3 | Left | Macroreentry | Mitral valve | CW |
| 4 | Left | Figure-of-eight | Left & right PVs | Anterior |
| 5 | Left | Figure-of-eight | Left & right PVs | Posterior |
| 6 | Left | Figure-of-eight | Right PVs | Anterior |

The second step was the creation of the edge between each node $i$ and $j \in \mathcal{B}_i$. To do so, we estimated the conduction velocity (CV) between the two nodes through their activation time delay and distance between them. In case the CV was within a predefined physiological range, the directed edge was created. The estimate was performed by extracting a time window from $\tilde{\Phi}_{e,n}$, time-referenced to each QRS complex (from the simultaneously recorded surface ECG) and evaluated whether a pair of electrodes was close enough to nodes $i$ and $j$ and not moving (up to a tolerance of 2 mm). The time window was set as the average beat-to-beat time interval. A cross-correlation-based algorithm was then applied between the signals associated to the two electrodes to find their delay. Given the fact that many QRS complexes were available, we estimated a set of delays for each pair of nodes. A $t$-test was then applied to verify whether the delay was statistically significantly different than 0. If so, the CV was estimated as the ratio of the distance between the nodes $i$ and $j$ and the average time delay. As such, the algorithm works directly on the unipolar electrograms and does not rely on preprocessed local activation time maps.

To further increase the robustness of the network, we repeated its creation 4 times after sliding the time window (the overlap between consequent windows was set to 100 ms). The 5 networks were then consolidated to obtain the final one. All technical details of the implementation are reported in [5].

Compared to [5], here we improved the creation of the network by changing two parts of the overall algorithm. First, instead of uniformly sampling the nodes $V_{prop}$ and applying Delaunay triangulation to set the neighbors, we downsampled the original mesh using the Meshtool software [16]. This operation reduced the number of spurious connections between unconnected anatomical structures that were not present in the original mesh but added by the Delaunay triangulation. Second, we used the activity in the electrograms recorded in the coronary sinus (CS) as reference for the selection of the time window, rather than the QRS complex on surface ECG. In fact, referencing on the ventricular depolarization as we did in [5] was effective but had one main disadvantage: the time delay added by the atrio-ventricular node after being triggered by an atrial wave shows physiological variability, thus adding unnecessary errors to the estimate of the time delay between signals.

The output of this phase comprised two networks, *i.e.*, the directed network resembling the electrical propagation $G_{prop} = (V_{prop}, E_{prop})$ and the undirected network describing the downsampled triangular mesh $G_{mesh} = (V_{mesh}, E_{mesh})$. It is worth noting that the two networks shared the same nodes, *i.e.*, $V_{prop} = V_{mesh}$. Figure 1a depicts an example of both networks.

### 2.2. Detection of macroreentries

In [5], the network $G_{prop}$ described in the previous section was used to detect cycles using a standard depth-first search (DFS) algorithm. In network theory, a cycle is defined as a non-empty se-
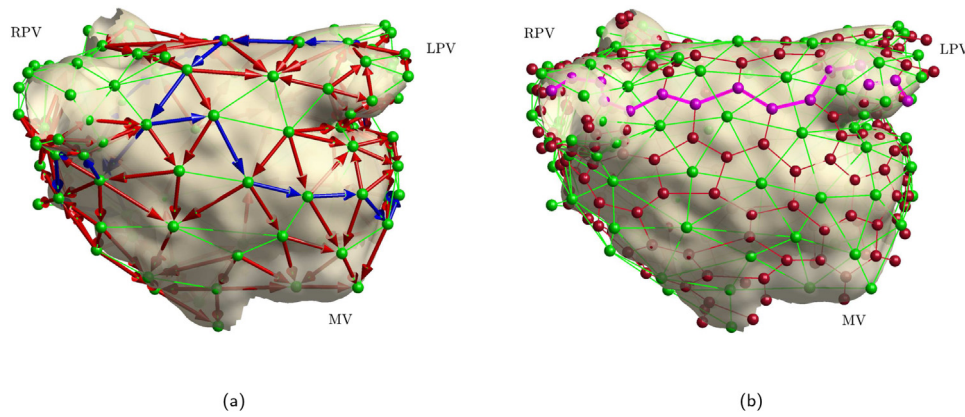
(a)                                                         (b)

**Fig. 1.** (a) Example of implementation of directed network mapping. Green spheres represent the nodes distributed on the atrial mesh while the green lines are the edges connecting neighboring nodes. Spheres and lines construct the graph $G_{mesh}$. Red arrows indicate the directed connection between two neighboring nodes as a model of electrical propagation. Spheres and arrows represent the graph $G_{prop}$. Blue arrows represent the macroreentries identified as they show a cycle. (b) The Voronoi tessellation $G_{lines}$ (red), built on top of $G_{mesh}$ (shown in green), is reported as red spheres and red lines. The purple line represents an example of an ablation line traversing along the edges of the Voronoi tessellation. The atrial model is the clinical case 9 of Table 2.

**Table 2**
Complete list of analyzed clinical CAT cases.

| No. | Atrium | Suspected mechanism | Description and treatment |
|---|---|---|---|
| 1 | Right | Tricuspid valve reentry CCW | The mechanism interrupted after ablating the CTI. |
| 2 | Right | Tricuspid valve reentry CCW | The mechanism interrupted after ablating the CTI. |
| 3 | Left | Mitral valve reentry CW | The patient previously received a PVI and an anterior block line from MV to LSPV. A gap was detected in the anterior block line. The mechanism interrupted after closing the gap. |
| 4 | Left | Mitral valve reentry CW | The patient was previously treated with a PVI, a posterior roof block from LSPV to RSPV and an anterior line from the MV to LSPV. A gap was detected in the anterior block line. The mechanism interrupted after closing the gap. |
| 5 | Left | Mitral valve reentry CW | The patient had a previous PVI. Gaps were found in the previous PVI. The mechanism stopped with a MIL connecting the MV and the LSPV isolation. |
| 6 | Left | Microreentry around PVI | The patient had a previous PVI. Gaps were found in both left and right PVI of the previous ablation. The mechanism was stopped after closing the gaps in the previous left PVI. The gap on the right side was closed too. |
| 7 | Left | Figure-of-eight macroreentry around left and right PVs | The patient had a previous PVI. Gaps were found in both left and right PVIs of the previous ablation. The mechanism was stopped after a roof line. A reisolation of the LIPV, RIPV and RSPV was also performed. |
| 8 | Left | Figure-of-eight macroreentry around left and right PVs | Patient had received a previous PVI. Small areas of block in septal area were identified. The mechanism stopped with a roof line. |
| 9 | Left | Figure-of-eight macroreentry around left and right PVs | The patient had a previous PVI. Gaps were found in both left and right PVI of the previous ablation. The mechanism stopped after closing the gaps in the PVI. The patient was also treated with a roof line. |
| 10 | Left | Macroreentry around right PVs | The patient was previously treated with a PVI and an anterior block line from MV to LSPV. Gaps were detected in the right PVs and anterior block line. The mechanism stopped after closing the gap in the anterior line. |

quence of nodes linked by directed edges in which the first and last node coincide. In our context, a cycle represented an electrical reentry activity. However, we noticed that a few macroreentries were not identified because a single edge was missing in the directed network. In order to mitigate this problem (possibly occurring in longer cycles), in this study, a new algorithm for cycle detection tolerant to gaps of a single edge was developed. In particular, we leveraged the fact that the DFS algorithm was very efficient in finding cycles.

The algorithm works as follows. Given a node $i$ in $V_{prop}$, the directed edges connecting each node in $\mathcal{B}_i$ with $i$ were temporary set, and the DFS algorithm was run in this modified network to find the cycles. This step was repeated for all the nodes in $V_{prop}$ and all cycles found were merged. The algorithm was able to detect the macroreentries previously missed. The drawback of this procedure was the identification of many cycles similar to each other. For visualization purposes, all cycles were clustered into groups using the same graph-based clustering technique reported in [5] with a threshold of 0.7.

Figure 1a depicts an example of detected cycles.

### 2.3. Ablation lines

The networks $G_{prop}$ and $G_{mesh}$ could be leveraged to study the effect of ablation lines on the atrial tissue. To do so, a third undirected network $G_{lines} = (V_{lines}, E_{lines})$ derived from $G_{mesh}$ was first built as follows. Each triangle in the mesh was used to create the set of nodes $V_{lines}$. In other words, each triangle in the mesh defined a specific node in $V_{lines}$. The position of these nodes on the atrial model was defined as the centroid of each triangle. For a triplet of nodes in $V_{mesh}$, $i$, $j$ and $z$ with $j, z \in \mathcal{B}_i, i \neq j \neq z$, the position was $(\mathbf{p}_i + \mathbf{p}_j + \mathbf{p}_z)/3$.

The edges $E_{lines}$ were created by connecting nodes of $V_{lines}$ of adjacent triangles (*i.e.*, triangles sharing two nodes). The resulting graph was a Voronoi tessellation built on top of the triangular mesh $G_{mesh}$. This graph represents a reticulum of possible ablation lines. In other words, an ablation line was then defined as a path on $G_{lines}$. Figure 1b shows the Voronoi tessellation of possible ablation lines.

The Voronoi tessellation contained a set of possible ablation lines lying within the atrial surface but not touching the bound-

aries of the model. In other words, no line was actually interrupting the electrical propagation traveling along anatomical regions such as mitral valve (MV), PVs, *etc.*, due to the fact that the regions were on the boundaries of the anatomical model. In order to equip the Voronoi tessellation with ablation lines possibly interrupting such electrical propagations, all nodes on the free boundaries were identified. Then, for each triangle having two nodes located on a free boundary, a new node was added in $V_{\text{lines}}$ and its position was mirrored with respect to the centroid of the triangle. This approach ensured that all edges in $G_{\text{mesh}}$ had their corresponding ablation edge in $G_{\text{lines}}$. The total number of nodes of $G_{\text{lines}}$ was $M_A$. An example of these nodes is reported in the lower part of Fig. 1b.

Another important aspect for the addition of new nodes in $V_{\text{lines}}$ was the possibility to determine which nodes in $V_{\text{mesh}}$ were located on the valves and PVs. This was achieved by identifying the connected components in the graph built only using the nodes of the free boundaries. The association between the nodes in the free boundary and the added nodes in $V_{\text{lines}}$ was then straightforward. Associating the correct anatomical structure (*e.g.*, MV) to a connected component was done by visual inspection in this study.

The main advantage of this procedure is that each edge in $G_{\text{lines}}$ crosses exactly one edge on $G_{\text{mesh}}$ and this property was leveraged to determine whether an ablation line would interrupt a cycle in $G_{\text{prop}}$. In particular, we were able to define the function

$$\text{cut1edge} : (e_a, e_m) \in E_{\text{lines}} \times E_{\text{mesh}} \to \{0, 1\} \tag{1}$$

where the value of the function cut1edge is 1 when the edge $e_a$ in $E_{\text{lines}}$ cuts the edge $e_m \in E_{\text{mesh}}$, 0 otherwise.

In our study, among all possible paths on the Voronoi tessellation, we considered the ablation lines with the shortest path between each pair of nodes belonging to the i) MV and left PVs; ii) MV and right PVs; iii) left PVs and right PVs for the left atrium and for the right atrium; iv) inferior vena cava and superior vena cava; v) inferior vena cava and tricuspid valve; and vi) superior vena cava and tricuspid valve.

## 2.4. Recommender system

Once the directed network $G_{\text{prop}}$, the mesh $G_{\text{mesh}}$ and the Voronoi tessellation $G_{\text{lines}}$ were created, it was possible to define an algorithm able to recommend ablation lines suitable to interrupt all reentry activities identified as cycles.

All identified cycles were stored as a set

$$\mathcal{L} = \{L_1, L_2, \ldots, L_{\#\mathcal{L}}\} \tag{2}$$

where $\#\mathcal{L}$ is the total number of cycles and each $L_i$ is a directed graph containing only one cycle. The nodes of each element $L_i$ were the same of $G_{\text{mesh}}$.

All possible ablation lines built upon the Voronoi tessellation were stored as a set

$$\mathcal{A} = \{A_1, A_2, \ldots, A_{\#\mathcal{A}}\} \tag{3}$$

where $\#\mathcal{A}$ is the total number of ablation lines and each $A_i$ is an undirected graph containing only one ablation line. The nodes of each element $A_i$ were a subset of $G_{\text{lines}}$.

We denote the graphs of a specific cycle $L_j$ and ablation line $A_i$ as $(V_{\text{prop},L_j}, E_{\text{prop},L_j})$ and $(V_{\text{lines},A_i}, E_{\text{lines},A_i})$, respectively.

The main objective was to find the optimal set of ablation lines to stop the CAT. In this study, we considered the set able to interrupt all cycles in $\mathcal{L}$ with minimum ablation length as optimal.

The optimization problem was designed as follows. First, let us define $\mathcal{C} \subseteq \mathcal{A}$ (*e.g.*, $\mathcal{C} = \{A_2, A_5, A_8\}$) as the set representing possible candidate ablation lines. From this candidate set, the overall ablation length was defined as follows. Considering that the elements of $\mathcal{A}$ are all graphs, each $A_i$ has its associated set of edges $E_{\text{lines},A_i}$.

Let then construct the set of edges $E_{\mathcal{C}}$, as follows:

$$E_{\mathcal{C}} = \bigcup_{A_i \in \mathcal{C}} E_{\text{lines},A_i} \tag{4}$$

The edge set $E_{\mathcal{C}}$ contained the edges of all $A_i$ in the candidate set $\mathcal{C}$.

The overall ablation line length was then defined as

$$l_{\mathcal{C}} = \sum_{e \in E_{\mathcal{C}}} d(e) \tag{5}$$

where $d(e)$ is the length of edge $e$ in mm.

The second step of the algorithm was to define how many cycles were interrupted by the candidate set $\mathcal{C}$. To do so, by leveraging the Voronoi tessellation previously created, it was possible to define the function cut that indicated whether a given ablation line $A$ would interrupt a certain cycle $L$, as follows.

$$\text{cut} : (A, L) \to \{0, 1\} \tag{6}$$

where the output 1 means interruption, 0 otherwise. Formally, if $\exists (e_A, e_L) \in E_{\text{lines},A} \times E_{\text{prop},L}$ such that cut1edge$(e_A, e_L) = 1$, then the output was set to 1. Using this function, it was possible to define an additional set $\mathcal{T}_A$ containing all cycles interrupted by a given ablation line $A$, as follows

$$\mathcal{T}_A = \{L : L \in \mathcal{L}, \text{cut}(A, L) = 1\} \tag{7}$$

By leveraging this set, the number of cycles interrupted by the ablation lines stored in the candidate set $\mathcal{C}$ can be defined as

$$r_{\mathcal{C}} = \#\left(\bigcup_{A \in \mathcal{C}} \mathcal{T}_A\right) \tag{8}$$

Finally, the overall optimization problem was defined as

$$
\begin{array}{ll}
\text{find all sets} & \mathcal{C} \\
\text{that minimize} & l_{\mathcal{C}} \\
\text{subject to} & r_{\mathcal{C}} = \#\mathcal{L}
\end{array}
\tag{9}
$$

## 2.5. Heuristic

The number of possible candidate set $\mathcal{C}$ for the problem in (9) is large and grows exponentially with the number of ablation lines in $\mathcal{A}$. Precisely, it is

$$\sum_{k=1}^{\#\mathcal{A}} \binom{\#\mathcal{A}}{k} = 2^{\#\mathcal{A}} - 1. \tag{10}$$

The computational complexity $\mathcal{O}(2^{\#\mathcal{A}})$ suggested that enumerating all possible solutions and evaluating them according to (9) was feasible only for a low number of ablation lines.

In this study, we developed a heuristic that can guide the identification of a local optimal candidate set when the number of ablation lines is large. The main idea of the algorithm is to add one optimal ablation line at a time to a set of already established ones using an iterative approach, with an initially empty set. Thus, the optimization problem was solved by splitting it into two sequential problems. The first one determines the subset of all candidates (including the previously selected lines) that maximizes the number of cycles interrupted. Then, among the candidates of the subset, the candidate adding the shortest ablation line to the overall ablated surface is selected (in case of multiple candidates, though very unlikely, a random ablation line was selected among those with equal performance).

The algorithm was stopped when at least one candidate set $\mathcal{C}^*$ interrupted all cycles or when a maximum number of ablation lines, here called "depth", was reached. Using this approach, the number of candidates $\mathcal{C}$ to evaluate reduces heavily to

$$\sum_{i=0}^{\text{depth}-1} (\#\mathcal{A} - i) = \frac{\text{depth}(2\#\mathcal{A} - \text{depth} + 1)}{2} \tag{11}$$

that reaches $\#\mathcal{A}(\#\mathcal{A}+1)/2$ when depth $= \#\mathcal{A}$. The complexity of the heuristic-based algorithm is polynomial, i.e., $\mathcal{O}(\#\mathcal{A}^2)$ or $\mathcal{O}(\text{depth}^2)$.

Algorithm 1 reports the pseudocode of the algorithm.

---

**Algorithm 1** Pseudocode of the proposed heuristic aiming to recommend the ablation strategy.

---

**Require:** $\mathcal{A}$, $\mathcal{L}$, depth $\in \mathbb{N}_+$
  $\mathcal{C}^* \leftarrow \{\}$
  $i \leftarrow 1$
  **while** $r_{\mathcal{C}^*} < \#\mathcal{L}$ **and** $i \leq$ depth **do**
      $\mathcal{P} \leftarrow \{\mathcal{C} : \mathcal{C} \subseteq \mathcal{A}, \#\mathcal{C} = i, \mathcal{C}^* \subseteq \mathcal{C}\}$
      $\mathcal{P}^{\max} \leftarrow arg\,max_{\mathcal{C} \in \mathcal{P}} r_{\mathcal{C}}$
      **if** $\nexists \mathcal{C} \in \mathcal{P}^{\max}$ **having** $r_{\mathcal{C}} > r_{\mathcal{C}^*}$ **then**
          **Exit**
      **end if**
      $\mathcal{P}^{\max/\min} \leftarrow arg\,min_{\mathcal{C} \in \mathcal{P}^{\max}} l_{\mathcal{C}}$
      $\mathcal{C}^* \leftarrow$ **random pick from** $\mathcal{P}^{\max/\min}$
      $i \leftarrow i + 1$
  **end while**

---

### 2.6. Data

#### 2.6.1. Simulations

We validated the recommender system in simulated CAT scenarios of atrial flutter (AFL). To do so, we repeated the simulations of 6 different AFL mechanisms investigated in a recent study [9]. These simulations included both right and left forms of AFL, such as macroreentries around the valves and across the roof. A complete list of scenarios is provided in Table 1.

The objective of the simulations was the verification that the recommended ablation lines would stop the AFL mechanism in place. On the simulated data, the recommender system was run and then the optimal ablation lines were identified on $G_{\text{lines}}$. Each line $A \in \mathcal{C}^*$ was then projected on the original atrial mesh by identifying the nearest node from each one in $V_{\text{lines},A}$. The boundary nodes of $A$ were then connected to the closest node belonging to one of the anatomical structures (identified again with the free boundary algorithm). All nodes were connected using the shortest path algorithm. The respective ablation lines identified were then virtually applied to each of the 6 AFL scenarios to verify the interruption of the AFL mechanism. Interruption of the mechanism was considered successful if 3 s after the application of the ablation line the electrical propagation had ceased.

Simulations were generated as follows. Cardiac excitation was modeled using the multifrontal fast marching approach to solve the isotropic Eikonal equation [17–19]. The atrial electrophysiological activity was simulated on the tetrahedral volumetric mesh of a bi-atrial anatomy, generated from segmented magnetic resonance imaging data of a healthy subject [20]. Inter-atrial connections and fiber orientation were generated by a rule-based algorithm [21,22]. Scars were added circumferentially around ipsilateral pulmonary veins representing ablation scars from the previous pulmonary vein isolation intervention. The recommended ablation lines were mapped from the surface mesh to the volumetric mesh considering the 20 closest neighbors to obtain an ablation of finite size. The simulations were initiated by manually placing triggers and refractory areas.

#### 2.6.2. Clinical cases

The recommender system was tested on 10 patients (age: $66 \pm 5$ years; male/female: 7/3) with CAT who underwent an EP study and catheter ablation. The subjects retrospectively selected by the clinicians were all complex AFL cases who had a history of AF or one previous PVI. The study was performed using a 64 mini-electrode small basket array (IntellaMap Orion$^{\text{TM}}$, Boston Scientific, Inc., Malborough, USA) that enabled rapid high-density mapping. The cases were provided by Städtisches Klinikum Karlsruhe, Germany and included 2 AFL scenarios in the right and 8 in the left atrium. Data collection was performed according to the Helsinki Declaration guidelines on human research. The research protocol used in this study was reviewed and approved by the local review board. All patients provided written informed consent.

Each CAT case was analyzed offline, after the intervention, by directed network mapping to create the propagation network. Only data collected before the actual ablation were analyzed. Macroreentries were identified using the algorithm tolerant to one missed edge described in Section 2.2. Only cycles having $\geq 10$ nodes (average length $\geq 136$ mm, sufficient according to Ho et al. [23]) were considered as macroreentries. The recommender system was then employed to recommend the set of ablation lines needed to interrupt all cycles.

The performance of the recommender system was assessed by visual inspection of the suggested ablation lines by the expert clinician of our team. The performance of the recommender system was assessed with two different approaches. The first approach evaluated whether the recommended lines matched the ones performed to terminate the mechanism in the EP lab. The second approach considered the recommendation as correct in case the lines were located in the expected anatomical position according to the guidelines for the treatment of the CAT mechanism.

It is worth noting that the case 6 presented only microreentries around the PVs. Instead of excluding this case, we wanted to assess the potential of our algorithm for the recommendation of ablation lines suitable for microreentries as well. To do so, we first identified microreentries using the DFS algorithm without tolerance on missing edges (see Section 2.2), with cycles containing less than 10 nodes. Regarding the set $\mathcal{A}$ of ablation lines, we identified all ablation paths between nodes of the Voronoi tessellation that were no more than 3 nodes away from the free boundaries of the PVs. Recommendations were obtained for case 6 on this set of ablation lines.

Table 2 reports the list of all cases analyzed with the algorithm.

## 3. Results

Directed network mapping was performed on the simulated AFL episodes using the updated algorithm. In all scenarios, the mechanism was properly identified. The recommended ablation lines for the scenarios from 3 to 6, i.e., MV and figure-of-eight macroreentries, successfully interrupted the mechanism. The first and second, i.e., tricuspid valve macroreentries, converted into a biatrial AFL.

Directed network mapping was recomputed for all clinical cases to assess whether the modifications implemented improved the detection of the macroreentries with respect to our previous study [5]. Differently than before, macroreentries of case 5, 8, and 9 were now properly detected. All other cases remained unaltered. In summary, only cases 3 and 10 were partially identified. These modifications led to an overall accuracy of about 80%. The number of nodes distributed by the downsampling algorithm was $114(107, 136)$ [median (interquartile range)]. Fig. 2c, e and f show the macroreentries newly identified for three out of four cases, while Table 3 reports a summary of the results. Among all cycles in a given group, only the cycle having the minimum average Menger curvature is plotted.

The first two clinical cases (1 and 2) were typical counterclockwise AFL with a critical inferior turning point between the tricuspid ring and the inferior vena cava (IVC) known as the cavotricuspid isthmus (CTI). Directed network mapping detected 46 different cycles in case 1, and 183 in case 2, with two groups identified
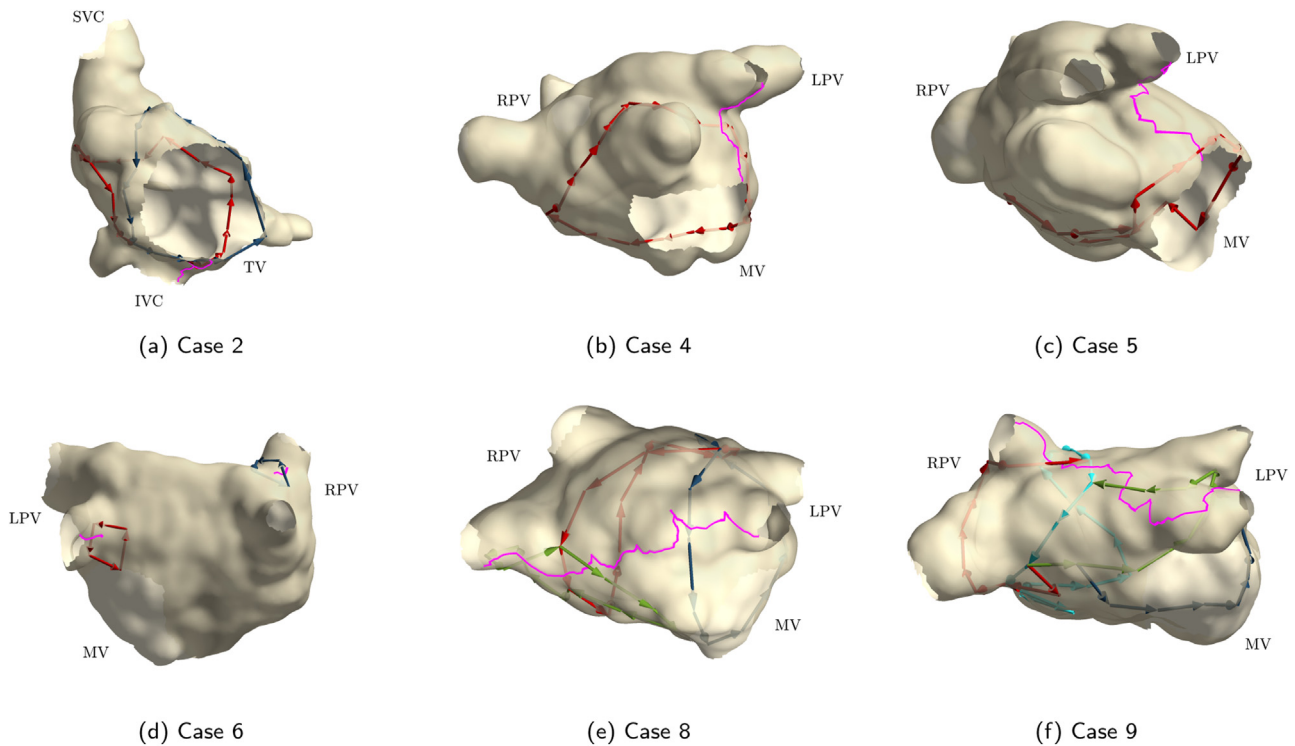
(a) Case 2

(b) Case 4

(c) Case 5

(d) Case 6

(e) Case 8

(f) Case 9

**Fig. 2.** Results of the recommender system for 6 clinical cases. Arrows depict the reentry identified by directed network mapping with arrow colors representing cycles of different groups. Among all cycles in a group, only the one with a minimum average Menger curvature is reported. The purple line represents the recommended ablation line. Panels a), b), c), d), e) and f) correspond to case 2, 4, 5, 6, 8 and 9 of Table 2.

**Table 3**

Summary of the results for the clinical cases. For each of the ten patients, column 2 reports the number of loops and groups of loops identified with the methodology reported in [5], column 3 reports the loops and groups identified with tolerance on 1-edge gap, $\#\mathcal{A}$ is the number of possible ablation lines, $\#\mathcal{C}^*$ is the number of ablation lines which stop all identified reentries, $l_{\mathcal{C}^*}$ is the length of the ablation lines contained in $\mathcal{C}^*$ and the last column reports the computational time for obtaining the recommendation. For case 6, † refers to results related to microreentries.

| No. | $\#\mathcal{L}$, #groups | $\#\mathcal{L}$ with 1-edge gap, #groups | $\#\mathcal{A}$ | $\#\mathcal{C}^*$ | $l_{\mathcal{C}^*}$ (mm) | Time (s) |
|---|---|---|---|---|---|---|
| 1 | 4, 1 | 46, 2 | 271 | 1 | 28 | 5.9 |
| 2 | 13, 2 | 183, 2 | 255 | 1 | 31 | 34.5 |
| 3 | 0, 0 | 20, 2 | 614 | 1 | 36 | 8.8 |
| 4 | 0, 0 | 17, 1 | 584 | 1 | 38 | 8.2 |
| 5 | 0, 0 | 9, 1 | 454 | 1 | 62 | 2.2 |
| 6 | 4, 2† | - | 3315† | 2† | 14† | 12.7† |
| 7 | 21, 3 | 310, 5 | 503 | 2 | 172 | 295.2 |
| 8 | 0, 0 | 76, 3 | 668 | 1 | 113 | 28.6 |
| 9 | 4, 1 | 63, 4 | 479 | 1 | 91 | 16.2 |
| 10 | 0, 0 | 9, 2 | 532 | 1 | 62 | 3.4 |

for both cases, a cycle group around the tricuspid valve and another one around the IVC. This was in line with what was found in simulation 1 and 2. The numbers of possible ablation lines were 271 and 255, respectively. The optimal ablation line for both cases was along the CTI. The lengths of the optimal ablation lines were 28 mm (case 1) and 31 mm (case 2). Figure 2a reports the results of case 2 (Figure for case 1 is reported in the supplementary material).

Cases 4 and 5 displayed left atrial reentries around the MV in clockwise direction. Directed network mapping detected 17 different cycles in case 4 and 9 in case 5, respectively. In both cases, a single group of cycles around the MV was found. The numbers of possible ablation lines were 584 and 454, respectively. The optimal ablation line for both cases was the line connecting the MV with the left PVs, which is called endocardial mitral isthmus line (MIL). The lengths of the optimal ablation lines were 38 mm for case 4 and 62 mm for case 5. Figure 2b and c show the cycles identified for these two cases, respectively.

Case 6 had microreentries due to gaps in the previous PVI, in both left and right PVs. Directed network mapping detected 4 cycles, with either 3 or 4 nodes, belonging to two different groups: one group near the left superior PV (LSPV) and the other one near the right inferior PV (RIPV). The number of possible ablation lines was 3315. The ablation lines identified were two: one for each left and right PVs. These ablation lines pointed to the possible gaps in the previous PVI ablation. Figure 2d reports the results for case 6.

Case 7 displayed a figure-of-eight macroreentry around both left and right PVs. Directed network mapping found 310 cycles in this case. Figure-of-eight was properly identified. Additional cycles with ≥ 10 nodes were found traveling around both right PVs individually. The number of ablation lines was 503. The optimal ablation line for this case connected the left PVs to both right PVs using two paths (Figure for this case is reported in the supplementary material). The length of overall ablation line was 172 mm.

Cases 8 and 9 had confirmed figure-of-eight macroreentries. Directed network mapping detected 76 cycles in case 8 and 63 in

case 9. In both cases, the algorithm correctly detected the propagation pattern around the PVs. Here, we found various cycle groups, which included cycles around left and right PVs, as well as cycles around the individual PVs, not as a pair. The number of ablation lines were 668 and 479 for cases 8 and 9, respectively. The optimal ablation line for both cases was the one connecting the left pair of PVs to the right pair of PVs. The lengths of the optimal ablation lines were 113 mm for case 8 and 91 mm for case 9. Figure 2e and f report the results for the case 8 and 9, respectively.

The mechanisms of cases 3 and 10 were partially identified (please, refer to the supplementary material for their visualizations). For case 3, directed network mapping detected 20 different cycles but none of them was found around the MV. Two groups of cycles were detected around the left PVs in counterclockwise direction. Despite the partial identification, we ran the recommender system in this case too. The number of possible ablation lines was 614. A single optimal ablation line was recommended to connect the MV to the left PVs. The length of the ablation line was 36 mm. For case 10, directed network mapping reported a macroreentry around right PVs. Here, it found two groups of cycles, both revolving only around the RIPV in a sort of concentric fashion. The mechanism was coherent with respect to the side of the reentry but no reentrant activity was clinically observed in the inferior right PV. In addition, it failed to identify the gap in the anterior line responsible for the macroreentry. The number of ablation lines was 532. The optimal ablation line connected the left pair of PVs to the right pair of PVs. The length of the line was 62 mm.

All cases but cases 6 and 7 needed only one ablation line to interrupt all reentries, whereas cases 6 and 7 required two lines each.

Overall, on clinical data, the recommended ablation lines were matching the ones performed by the clinician in 67% of the cases, while they were located in the expected anatomical position in 89% of the cases.

The execution time for running the heuristic was traced for all cases. On a MacBook Pro 2.3 GHz 8-Core Intel Core i9 16 GB 2667 MHz DDR4 using Matlab (R2021a, The MathWorks, Inc., Natick, USA), the execution time was $10.8(5.9, 28.6)$ s [median (interquartile range)].

Table 3 reports a summary of the results on the clinical cases.

## 4. Discussion

### 4.1. Improvements of directed network mapping

With respect to our previous work [5], directed network mapping was improved by two major modifications. First, the mesh was downsampled instead of creating a Delaunay triangulation from the selected nodes on the mesh. Considering that both $G_{prop}$ and $G_{lines}$ are built on top of $G_{mesh}$, this step is clearly fundamental. On the one hand, the downsampling procedure prevented spurious connections between anatomical regions that were not actually connected (*e.g,* between the body of the left atrial appendage and the LSPV). The algorithm adapted automatically the position of the nodes and their number to preserve the original shape. On the other hand, this adaptation likely caused the false negatives (*i.e.,* cycles not detected) of most of the macroreentries when the DFS algorithm did not tolerate gaps (column #$\mathcal{L}$ in Table 3). In fact, in our previous work, the number of nodes spread on the mesh was set to 100 for all clinical cases, which is, on average, 15% less than what was allocated by the downsampling algorithm. As reported in [5], the higher the number of nodes, the higher the probability that a "broken" cycle would appear. Such observation was also supported by the number of cycle groups found after introducing the tolerance regarding 1-edge gaps (column #groups in Table 3),

which confirmed the mechanisms in place without producing false positives.

The second modification involved the change of the time reference used for the creation of the network. In our previous study [5], we employed the surface QRS complex while here we used the activation of the CS. Referencing on the CS is commonly preferred over the QRS complex due to a lower error achieved during sequential mapping. In addition, this allowed to leverage the information available from all atrial activations, with the downside of increasing the computational time required by directed network mapping.

The 1-edge gap algorithm was an additional improvement on top of directed network mapping. It was found to increase the total number of cycles detected (column #$\mathcal{L}$ with 1-edge gap in Table 3). Yet, the newly found cycles were all similar to each other, due to the fact that only one edge was possibly added. This fact was reflected in the number of cycle groups identified, that did not change markedly compared to no tolerance on missing edges, but improved the overall identification of the mechanisms up to 80%.

### 4.2. Comparison between recommended ablation lines and clinical treatment

The recommender system was found able to recommend ablation lines, for the CAT considered in this study, that were partially matching those performed clinically. In particular, for the cases displaying typical AFL (case 1 and 2), the optimal ablation line was along the CTI, which is the standard treatment for typical flutter [24], and they matched what performed clinically for these two cases.

For MV reentries (cases 3, 4 and 5), the recommended ablation line was the MIL in all cases. This line is what typically performed for the treatment of this reentry [25]. Despite the mechanism of case 3 was partially detected, it is worth noting that directed network mapping correctly identified the gap in the anterior block line, that was responsible for the mechanism in place. The ablation line recommended was resembling the MIL at the posterior mitral isthmus, that is considered a conventional MIL [25]. Similar results were obtained for case 4 and 5 in which MILs to LSPV and LIPV were recommended. Despite these lines were coherent with the mechanism, the treatment that stopped the reentry in cases 3 and 4 involved the closing of the gap in the MIL previously performed from the mitral annulus to the LSPV. For case 5, the recommendation was correct. Furthermore, anterior MIL is typically preferred over the posterior one since it is easier to achieve a bidirectional block with a lower length of the MIL [25]. However, the length of the line depends on the specific patient's anatomy and, other factors, such as the thickness of the myocardium and closeness to other anatomical structures, may play a role for the selection of what line to perform [26]. Therefore, the modeling of previous ablated tissue, thickness of the myocardium and preferences of ablation strategies in the optimization problem may represent additional steps to further improve the performance of the recommender system. We leave this investigation for future works.

Regarding the missed mechanism around the MV for case 3, we detected, by visual inspection, that a few edges around the annulus were not built by the algorithm, while most of other nodes resembled a cycle around the valve. We found that the histogram of the temporal delays between nodes in the disconnected region displayed a bimodal distribution with positive and negatives delays (and some with a peak around 0 ms as well). The respective modal delays had a CV within the range to construct the edge, however, the *t*-test failed due to an average delay close to 0 ms. A hypothesis to explain this phenomenon could be related to the presence of slow conductive areas in the surrounding of the gap in the anterior line. These areas might have created a periodic oscillation of

the delays of two neighboring nodes with respect to the CS activation. We leave the investigation of this hypothesis for future works.

For the figure-of-eight cases (7, 8, 9), the optimal line was the one connecting left and right PVs, resembling a roof line, a floor line or a combination of the two. Case 7 was found to require the most complicated ablation strategy according to our algorithm. In fact, the figure-of-eight mechanism also involved gaps in the previous PVI on the right PVs. Directed network mapping identified a reentry on each right PV. However, only a reentry on the RIPV was clinically observed. The mechanism was stopped by performing a roof line. In addition, PVI was also repeated. Despite the recommended strategy may look overly complicated, a closer inspection hints that a roof line and PVI on the right PVs were the necessary lines and matched with the actual ablation. The mechanism of the case 8 was stopped with a roof line, which matched to the recommended strategy. Regarding case 9, the patient had gaps in the previous PVIs which, once closed, caused the termination of the mechanism. In addition, a roof line was performed to ensure a successful intervention, that matched the recommendation.

Case 10 presented a macroreentry around the right PVs due to a gap in the previous line connecting the mitral annulus and RSPV. When the gap was ablated, the mechanism stopped. In this case, the recommended line resembled a roof line and it was the shortest single path terminating the CAT according to our algorithm. This case opens up to an interesting discussion. Indeed, the anteromedial line connecting the right PV ostium and MV typically shows large lengths [26], and thus it likely becomes excluded from the set of eligible lines by the heuristic implemented. In addition, this line is close to the aortic sinus, which requires attention when ablating along this isthmus: the critical position of other structures was a property not modeled in our optimization problem. For this specific case, with a proper modeling of previous ablations, the recommended line would have been the closing of the gap as optimal strategy.

Finally, the recommended lines for the case displaying microreentries (case 6) were two short paths interrupting the cycles appearing on both left and right PVs. Despite the recommender system being designed only for the treatment of macroreentries, we wanted to evaluate the potential for microreentries too. For this case, however, the ablation lines found need to be considered as only indications for the necessary treatment, and not for their exact location. In fact, interrupting any edge composing the cycle would stop the microreentry. This suggests that the optimization problem should be adapted to consider criteria different than the length of the ablation in this context. Here, gaps were found during the intervention on both left and right PVIs very near to the mechanisms identified by directed network mapping. However, only the gaps on the left PVI resulted in an observed microreentry. The microreentry identified on the right PVI was mostly located within the RSPV and was likely caused by a combination of factors such as the gap on the right PVI and the substrate of the previously ablated tissue. The clinical treatment was the closing of the gaps in both left and right PVIs, as indicated by the interruption of the microreentries provided by the recommender system. Further investigations are needed in this context.

### 4.3. Performance of the recommender system

One key assumption of our methodology was that ablation lines could only stop the mechanism in place but not change it. However, this assumption might not hold in practice and for this reason we implemented computerized simulations to assess such possible switch of the mechanism. Out of the six simulations considered, only the scenarios involving typical atrial flutter switched into a biatrial flutter. Biatrial tachycardia is considered a rare form of reentrant arrhythmia and is found associated with scars on the septum [27]. Such scars create a block of the electrical propagation between the left and right atria, thus promoting a reentry traveling from the right to the left atrium through the CS, and from the left to the right atrium through the Bachmann's bundle on the way back (or viceversa). We noted that the ablation recommended was very close to the septum due to the particular position of the IVC in this reconstructed anatomy (please, refer to Figure 3 in [5] to inspect the 3D model). Likely, the position of the line in combination with this specific anatomy caused the switch into a biatrial flutter.

The performance of the recommender system can be summarized under different perspectives. First, the position of the recommended lines matched what typically expected by the mechanism in place in 89% of the cases (cases from 1 to 5 and 7-9; case 6 excluded). Second, the suggested lines exactly matched the clinical treatment in 44% (cases 1, 2, 7, 8), and partially matched in 22% (cases 5 and 9). Hence, accuracy ranged between 44% to 67% with the actual treatment. The drop in performance was associated to the lack of modeling of the previous ablated tissue (cases 3, 4, 9, 10) into the optimization problem and the selection of the LISP instead of LSPV when performing a MIL (case 5). Third, the recommended lines terminated the mechanism in 67% of the simulated scenarios (however, we believe that this percentage is underestimated considering that the wrong recommendation was for a rare form of arrhythmia in a single anatomy considered).

Another point worth discussing, possibly affecting the performance, was that the recommended ablation lines displayed a "zigzag" behavior with both low and high spatial frequency oscillations (*e.g.*, Fig. 2e). The low oscillations were mostly due to the strategy used for the creation of the Voronoi tessellation. Indeed, the use of the centroid in each of the triangles composing the downsampled mesh forced the ablation path to circumnavigate the nodes where the electrical potentials were quantified (Fig. 1b). This behavior can be solved by i) forcing the downsampling algorithm to produce a denser distribution of nodes; or ii) adding points within each triangle where the ablation path could go through. In our opinion, both strategies have advantages and disadvantages. In fact, adding nodes to $G_{prop}$ might compromise the detection of cycles due to higher chances of missing edges (similar to what is described above), while adding points for ablation lines would make $\#\mathcal{A}$ grow drastically, thus increasing the computational time required to find the optimal ablation set. Regarding the high spatial frequency oscillations, they are mostly due to the way the ablation lines were projected from the Voronoi tessellation to the original mesh. We believe that this is a minor problem that can be easily solved by smoothing the line using a low pass filter or a geometric snake for a triangular mesh [11,28]. We leave these investigations and improvements for future works.

### 4.4. Comparison with other approaches

Despite our study reports the first attempt for the use of graph theory to recommend the ablation strategy from data collected during interventions, at the best of our knowledge, only one study investigated a similar approach [14]. Zahid et al. proposed to use the "minimum cut" algorithm based on a flow network to predict optimal ablation targets for left AFL. They used data collected from EP studies and magnetic resonance imaging to create a mathematical model, comprising a geometry annotated with both healthy and fibrotic tissues, and a cellular model, to simulate the electrical propagation. A flow network was constructed on simulated data considering each volumetric element of the geometry as a node, and connecting adjacent nodes only when the CV was higher than a certain threshold (they used 100 cm/s). Once the network was created, the "minimum cut" algorithm was employed to interrupt the mechanisms.

The "minimum cut" algorithm is the dual problem of the so-called "maximum flow" problem, common in network theory. Briefly, this problem requires the assignment of a maximum capacity to each edge of a graph. The maximum flow from one node, called source, to another one, called sink, is computed as the maximum sum of the flows between all paths connecting the source and sink, according to the maximum capacity of each edge (a clear example is the road network from one city to another one where each road has a maximum capacity of cars). Finding the maximum flow between two nodes is equivalent of identifying the minimum sum of the flows through the edges that, when removed, would separate the network into two disjoint networks (in the road example is equivalent to finding the bottleneck during traffic jam).

There are three major differences between our approach and that of Zahid et al.. The first one is that all algorithms we proposed are based only on data collected during mapping and do not require computerized simulations. This is clearly advantageous under different perspectives. On the one hand, directed network mapping and recommender system require only two important assumptions: i) stationary electrical propagation; and ii) CV within a physiological range. Both assumptions are also required by the flow network implemented by Zahid et al., but with additional requirements such as availability of imaging data, and electrophysiological model of atrial cells and model of fiber orientation, specifically fitted on patient's data. Also, results can be obtained fully automatic and nearly real-time with our approach, while computerized simulations are (typically) computationally expensive. On the other hand, the main drawback of the recommender system is that the mechanism may turn into a more complicated pattern after performing the suggested ablation lines (as it occurred in our simulations of typical AFL). In this case, being able to simulate beforehand the effect of the recommended ablations using advanced computational models seems a reasonable and feasible approach to further improve the performance.

The second difference is that the "minimum cut" algorithm needs the selection of the source and sink, *i.e.*, two nodes of the network. This selection represents a major difficulty and can completely change the output of the algorithm, *i.e.*, the ablation strategy recommended. In fact, the source and sink are typically inputs of the optimization problem. However, we found no criteria for the *a priori* selection of these two nodes considering the physiological phenomenon in place.

Finally, the third major difference is that in the approach by Zahid et al. there is no guarantee that the set of minimum cuts would resemble the ablation lines established for the treatment of CAT. Indeed, the noise present on the recordings may make the nodes of the network with a low degree, *i.e.*, just a few edges inward and outward to and from a node. Hence, the noise will likely lead the "minimum cut" algorithm to find a set of ablation lines, as short as one edge, that are disconnected between each other, for the treatment of macroreentries.

### 4.5. Limitations and future works

The association between anatomical structures, such as valves, appendage and PVs, and nodes on the free boundaries was the only step not performed automatically by our software. This problem was tackled recently by means of different tools such as machine learning [29] or statistical shape models [30]. Since this step was not the main objective of the study, we leave the insertion of this automatic association in the overall pipeline as future works.

The recommended ablation lines were the solution of the proposed optimization problem, which involved $G_{mesh}$, $G_{prop}$ and $G_{lines}$. It is worth noting that the optimization problem can be reframed by only using $G_{prop}$. Indeed, the overall objective is to find which directed edges in $G_{prop}$ must be removed to interrupt the

reentry. However, this approach does not ensure that the edges removed are connected through a path and this path resembles the shortest. In other words, the optimization problem requires a set of constraints to provide a meaningful solution. In our study, the constraints were set in the form of $G_{lines}$, which, on one hand, ensured a feasible solution (from a clinical perspective) and, on the other hand, made the solution clearly interpretable (not only as a set of directed edges removed but a path). Perhaps, an alternative problem formulation without $G_{lines}$ would speed up the search of a feasible solution by removing the infrastructure created to enforce the set of possible ablation lines. We leave this investigation to future studies.

The set of ablation lines was restricted to those from the free boundary of one anatomical structure to that of another one in both atria. However, this approach might be suboptimal in case of previous PVI (as in our case) because the ablated tissue is not considered in the optimization problem. In other words, the proposed recommender system does not assume that a previous PVI was performed. This lack of information might have led the recommender system to suggest longer ablation lines than actually needed, *e.g.*, not connecting PVIs from left to right PVs for the treatment figure-of-eight macroreentries (see case 9 in Fig. 2f). The influence of ablated tissue on the recommended ablation strategy will be investigated in the future.

Another important limitation is that we did not consider focal activations in the optimization problem. Despite directed network mapping seems able to identify such activations by looking at the in-degree of the nodes [15], modeling how they should be handled by the recommender system is challenging. In the current framework, the most straightforward way would be considering the smallest closed-loop ablation placed around each node in the propagation graph and let the recommender finding the optimal solution. However, this approach may contrast with the optimization problem designed specifically for macroreentries. In fact, the algorithm could find many of these closed-loop ablations simply because they tend to reduce the overall ablation length while removing macroreentries as well. A similar problem occurs when dealing with microreentries. We leave the investigation on how to handle focal activations and microreentries in the optimization problem for future.

As described in Section 4.3, the main reason for the mismatch between lines recommended and those actually performed by the electrophysiologists was likely the lack of modeling of previous ablation lines. These lines were however present in most of our patients (Table 2), but the data at disposal did not include such information and therefore they did not enter into the optimization problem. Future investigations will be dedicated to find the optimal strategy to model previous ablation lines (for instance, by prioritizing re-ablation of previous sites). At this current stage, while the performance obtained were sufficiently good, the algorithm still requires improvements for patients with CAT before deployment into clinical practice. However, even though preliminary, the study demonstrated that graph-based methods may represent a valid tool for guiding the planning of the treatment.

Another important point is that the recommender system could be extended to consider additional criteria rather than just the length of the ablation line. For example, ablating in diseased areas (identified as areas with low bipolar voltage, reduced conduction velocity or late gadolinium enhancement [31]) might be preferred to ablating nearby healthy tissue. This may lead, for example, to preferring an anterior MIL to a lateral MIL [32].

Finally, both directed network mapping and recommender system may obtain a boost in their computational performance if their algorithms are written in a parallelized fashion. In fact, both algorithms process a specific function for pairs of objects independently. Directed network mapping defines a directed edge for each

pair of nodes that are neighbors, whereas the recommender system evaluates the goodness of the candidate set $\mathcal{C}^* \cup \mathcal{A}_i$ for each $i$. This approach is expected to reduce the computational time by the number of parallel jobs. However, identifying possible bottlenecks is not trivial and therefore we leave this investigation for future studies.

## 5. Conclusions

In this study, we proposed a recommender system, built as solution of an optimization problem, able to suggest the optimal ablation strategy for the treatment of CAT. The problem was designed on top of the output of a recent technology used to model the electrical propagation, *i.e.*, directed network mapping [4,5], that makes use of graph theory. The optimization problem modeled the optimal ablation strategy as that one interrupting all reentrant mechanisms while minimizing the ablated atrial surface.

Considering the exponential complexity of finding the optimal solution of the problem, we introduced a heuristic algorithm with polynomial complexity. The proposed algorithm was applied to both simulated and clinical data, achieving promising performance, nearly real-time.

In conclusions, the study may open up interesting scenarios for the application of graph theory for the treatment of CAT.

## Declaration of Competing Interest

The authors declare that the research was conducted in the absence of any commercial or financial relationships that could be construed as a potential conflict of interest.

## CRediT authorship contribution statement

**Muhamed Vila:** Conceptualization, Software, Writing – original draft. **Massimo W. Rivolta:** Conceptualization, Software, Writing – original draft. **Cristian A. Barrios Espinosa:** Software, Writing – original draft. **Laura A. Unger:** Data curation, Writing – original draft. **Armin Luik:** Data curation, Writing – original draft. **Axel Loewe:** Conceptualization, Writing – original draft. **Roberto Sassi:** Conceptualization, Writing – original draft.

## Acknowledgments

## Supplementary material

Supplementary material associated with this article can be found, in the online version, at doi:10.1016/j.cmpb.2023.107406.

## References

[1] G. Lee, P. Sanders, J.M. Kalman, Catheter ablation of atrial arrhythmias: state of the art, Lancet 380 (9852) (2012) 1509–1519, doi:10.1016/S0140-6736(12)61463-9.

[2] C.D. Cantwell, C.H. Roney, F.S. Ng, J.H. Siggers, S.J. Sherwin, N.S. Peters, Techniques for automated local activation time annotation and conduction velocity estimation in cardiac mapping, Comput. Biol. Med. 65 (2015) 229–242, doi:10.1016/j.compbiomed.2015.04.027.

[3] M. Saeed, O. Berenfeld, H. Oral, Phase Mapping of Human Atrial Fibrillation, John Wiley & Sons, Ltd, 2019, pp. 652–659.

[4] N. Vandersickel, E. Van Nieuwenhuyse, N. Van Cleemput, J. Goedgebeur, M. El Haddad, J. De Neve, A. Demolder, T. Strisciuglio, M. Duytschaever, A.V. Panfilov, Directed networks as a novel way to describe and analyze cardiac excitation: directed graph mapping, Front. Physiol. 10 (2019) 1138, doi:10.3389/fphys.2019.01138.

[5] M. Vila, M.W. Rivolta, G. Luongo, L.A. Unger, A. Luik, L. Gigli, F. Lombardi, A. Loewe, R. Sassi, Atrial flutter mechanism detection using directed network mapping, Front. Physiol. 12 (2021) 749635, doi:10.3389/fphys.2021.749635.

[6] E. Van Nieuwenhuyse, T. Strisciuglio, G. Lorenzo, M. El Haddad, J. Goedgebeur, N. Van Cleemput, C. Ley, A.V. Panfilov, J. de Pooter, Y. Vandekerckhove, R. Tavernier, M. Duytschaever, S. Knecht, N. Vandersickel, Evaluation of directed graph-mapping in complex atrial tachycardias, JACC Clin. Electrophys. 7 (2021) 936–949, doi:10.1016/j.jacep.2020.12.013.

[7] L. Sun, C. Yang, L. Zhang, Y. Chen, Z. Wu, J. Shao, A preliminary study on atrial epicardial mapping signals based on graph theory, Med. Eng. Phys. 36 (7) (2014) 875–881, doi:10.1016/j.medengphy.2014.03.011.

[8] S. Tao, S.F. Way, J. Garland, et al., Ablation as targeted perturbation to rewire communication network of persistent atrial fibrillation, PLoS ONE 12 (2017) 1–18, doi:10.1371/journal.pone.0179459.

[9] G. Luongo, S. Schuler, A. Luik, T.P. Almeida, D.C. Soriano, O. Dössel, A. Loewe, Non-invasive characterization of atrial flutter mechanisms using recurrence quantification analysis on the ECG: acomputational study, IEEE Trans. Biomed. Eng. 68 (3) (2021) 914–925, doi:10.1109/TBME.2020.2990655.

[10] G. Luongo, L. Azzolin, S. Schuler, M.W. Rivolta, T.P. Almeida, J.P. Martínez, D.C. Soriano, A. Luik, B. M"uller-Edenborn, A. Jadidi, O. D"ossel, R. Sassi, P. Laguna, A. Loewe, Machine learning enables noninvasive prediction of atrial fibrillation driver location and acute pulmonary vein ablation success using the 12-lead ECG, Cardiovasc. Digit. Health J. 2 (2) (2021) 126–136, doi:10.1016/j.cvdhj.2021.03.002.

[11] A. Loewe, E. Poremba, T. Oesterlein, A. Luik, C. Schmitt, G. Seemann, O. Dössel, Patient-specific identification of atrial flutter vulnerability–a computational approach to reveal latent reentry pathways, Front. Physiol. 9 (2019), doi:10.3389/fphys.2018.01910.

[12] P.M. Boyle, T. Zghaib, S. Zahid, R.L. Ali, D. Deng, W.H. Franceschi, J.B. Hakim, M.J. Murphy, A. Prakosa, S.L. Zimmerman, H. Ashikaga, J.E. Marine, A. Kolandaivelu, S. Nazarian, D.D. Spragg, H. Calkins, N.A. Trayanova, Computationally guided personalized targeted ablation of persistent atrial fibrillation, Nat. Biomed. Eng. 3 (11) (2019) 870–879, doi:10.1038/s41551-019-0437-9.

[13] C.H. Roney, M.L. Beach, A.M. Mehta, I. Sim, C. Corrado, R. Bendikas, J.A. Solis-Lemus, O. Razeghi, J. Whitaker, L. O'Neill, G. Plank, E. Vigmond, S.E. Williams, M.D. O'Neill, S.A. Niederer, In silico comparison of left atrial ablation techniques that target the anatomical, structural, and electrical substrates of atrial fibrillation, Front. Physiol. 11 (2020), doi:10.3389/fphys.2020.572874.

[14] S. Zahid, K.N. Whyte, E.L. Schwarz, R.C. Blake, P.M. Boyle, J. Chrispin, A. Prakosa, E.G. Ipek, F. Pashakhanloo, H.R. Halperin, H. Calkins, R.D. Berger, S. Nazarian, N.A. Trayanova, Feasibility of using patient-specific models and the "minimum cut" algorithm to predict optimal ablation targets for left atrial flutter, Heart Rhythm 13 (8) (2016) 1687–1698, doi:10.1016/j.hrthm.2016.04.009.

[15] M. Vila, S. Rocher, M.W. Rivolta, J. Saiz, R. Sassi, Directed network mapping approach to rotor localization in atrial fibrillation simulation, in: Annual International Conference of the IEEE Engineering in Medicine and Biology Society, 2021, pp. 730–733, doi:10.1109/EMBC46164.2021.9629911.

[16] A. Neic, M.A. Gsell, E. Karabelas, A.J. Prassl, G. Plank, Automating image-based mesh generation and manipulation tasks in cardiac modeling workflows using Meshtool, SoftwareX 11 (2020) 100454, doi:10.1016/j.softx.2020.100454.

[17] V. Jacquemet, An eikonal approach for the initiation of reentrant cardiac propagation in reaction–diffusion models, IEEE Trans. Biomed. Eng. 57 (9) (2010) 2090–2098, doi:10.1109/TBME.2010.2051156.

[18] J. Trächtler, T. Oesterlein, A. Loewe, E. Poremba, A. Luik, C. Schmitt, O. Döossel, Virtualizing clinical cases of atrial flutter in a fast marching simulation including conduction velocity and ablation scars, Curr. Dir. Biomed. Eng. 1 (1) (2015) 405–408, doi:10.1515/cdbme-2015-0098.

[19] E. Pernod, M. Sermesant, E. Konukoglu, J. Relan, H. Delingette, N. Ayache, A multi-front eikonal model of cardiac electrophysiology for interactive simulation of radio-frequency ablation, Comput. Graph. 35 (2) (2011) 431–440.

[20] M.W. Krueger, G. Seemann, K. Rhode, D.U.J. Keller, C. Schilling, A. Arujuna, J. Gill, M.D. O'Neill, R. Razavi, O. Dössel, Personalization of atrial anatomy and electrophysiology as a basis for clinical modeling of radio-frequency ablation of atrial fibrillation, IEEE Trans. Med. Imaging 32 (1) (2013) 73–84, doi:10.1109/TMI.2012.2201948.

[21] A. Wachter, A. Loewe, M.W. Krueger, O. Dössel, G. Seemann, Mesh structure-independent modeling of patient-specific atrial fiber orientation, Curr. Dir. Biomed. Eng. 1 (1) (2015) 409–412, doi:10.1515/cdbme-2015-0099.

[22] A. Loewe, M.W. Krueger, F. Holmqvist, O. Dössel, G. Seemann, P.G. Platonov, Influence of the earliest right atrial activation site and its proximity to interatrial

connections on p-wave morphology, Europace 18 (suppl_4) (2016) iv35–iv43, doi:10.1093/europace/euw349.

[23] S.Y. Ho, J.A. Cabrera, D. Sanchez-Quintana, Left atrial anatomy revisited, Circ. Arrhythm. Electrophys. 5 (1) (2012) 220–228, doi:10.1161/CIRCEP.111.962720.

[24] F.G. Cosío, Atrial flutter, typical and atypical: a review, Arrhythmia Electrophys. Rev. 6 (2) (2017) 55, doi:10.15420/aer.2017:5:2.

[25] T. Maurer, A. Metzner, S. Yen Ho, P. Wohlmuth, B. Reißmann, C. Heeger, C. Lemes, K. Hayashi, A.M. Saguner, J. Riedl, C. Sohns, S. Mathew, K.-H. Kuck, E. Wissner, F. Ouyang, Catheter ablation of the superolateral mitral isthmus line, Circ Arrhythmia Electrophys. 10 (10) (2017), doi:10.1161/circep.117.005191.

[26] Y. Cho, W. Lee, E.-A. Park, I.-Y. Oh, E.-K. Choi, J.-W. Seo, S. Oh, The anatomical characteristics of three different endocardial lines in the left atrium: evaluation by computed tomography prior to mitral isthmus block attempt, EP Europace 14 (8) (2012) 1104–1111, doi:10.1093/europace/eus051.

[27] A. Tolat, E. Clark, V. Naraparaju, J. Flack, Macro-reentrant single-loop biatrial flutter appearing as typical atrial flutter: case study and review, J. Innov. Cardiac. Rhythm. Manage. 11 (11) (2020) 4306–4312, doi:10.19102/icrm.2020.111106.

[28] Y. Lee, S. Lee, Geometric snakes for triangular meshes, Comput. Graph. Forum 21 (3) (2002) 229–238, doi:10.1111/1467-8659.t01-1-00582.

[29] T. Zheng, L. Azzolin, J. Sánchez, O. Dössel, A. Loewe, An automate pipeline for generating fiber orientation and region annotation in patient specific atrial models, Curr. Dir. Biomed. Eng. 7 (2) (2021) 136–139, doi:10.1515/cdbme-2021-2035.

[30] C. Nagel, S. Schuler, O. Dössel, A. Loewe, A bi-atrial statistical shape model for large-scale in silico studies of human atria: model development and application to ECG simulations, Med. Image Anal. 74 (2021) 102210, doi:10.1016/j.media.2021.102210.

[31] D. Nairn, M. Eichenlaub, B. Müller-Edenborn, H. Lehrmann, C. Nagel, L. Azzolin, G. Luongo, R. Figueras Ventura, B. Rubio Forcada, A. Colomer, T. Arentz, O. Dössel, A. Loewe, A. Jadidi, LGE-MRI for diagnosis of left atrial cardiomyopathy as identified in high-definition endocardial voltage and conduction velocity mapping, medRxiv (2022), doi:10.1101/2022.02.02.22269817.

[32] H. Lehrmann, A.S. Jadidi, J. Minners, J. Chen, B. Müller-Edenborn, R. Weber, O. Dössel, T. Arentz, A. Loewe, Novel electrocardiographic criteria for real-time assessment of anterior mitral line block, JACC Clin. Electrophys. 4 (7) (2018) 920–932, doi:10.1016/j.jacep.2018.03.007.